Materials Advances

ROYAL SOCIETY OF CHEMISTRY

PAPER

View Article Online
View Journal | View Issue

Cite this: *Mater. Adv.*, 2026, 7, 5065

XPCS at the microsecond frontier: diffusion of PEGylated nanoparticles in water

Nele N. Striker, [a] Florian Schulz, [b] Claudia Goy,[a] Jonathan Correa, [a] Adriana Simancas, [a] Francesco Dallari, [c] Daniele Marzi,[d] Randeer Pratap Gautam, [ae] Carlos Arauz-Moreno, [f] Robert P. C. Bauer,[a] William Chèvremont, [d] Marco Cammarata, [d] Heinz Graafsma, [a] Frédéric Caupin [g] and Felix Lehmkühler *[a]

Probing nanoscale transport in liquids under extreme thermodynamic conditions is essential for understanding soft matter and nanomaterials. However, accessing intrinsic microsecond dynamics of nanometre-sized objects remains challenging for synchrotron-based X-ray photon correlation spectroscopy (XPCS) because of limitations of coherent flux and detector repetition rates. Here, we investigate the diffusion of dilute polyethylene glycol (PEG)-coated gold nanoparticles dispersed in water over a wide temperature range, including water's supercooled regime using XPCS. The measured dynamics exhibit purely diffusive behaviour, with relaxation rates scaling as q^2, and the extracted diffusion coefficients quantitatively follow the Stokes–Einstein relation with no slip boundary condition. Viscosity values derived from nanoparticle motion agree with established literature data, confirming that PEGylated nanoparticles act as reliable nanoscopic viscosity probes without evidence of ligand shell compression or structural changes. Using event-based XPCS with next-generation detectors, we access microsecond dynamics approaching the intrinsic Brownian timescale of nanometer-sized particles. These results establish PEGylated gold nanoparticles as robust probes of nanoscale transport and demonstrate the capability of advanced XPCS instrumentation to investigate fast dynamics in soft and nanoscale materials.

Received 18th March 2026,
Accepted 21st April 2026

DOI: 10.1039/d6ma00387g

rsc.li/materials-advances

1 Introduction

Water-based soft matter systems – such as colloidal dispersions, polymer solutions, hydrogels, and biological macromolecules – exhibit complex dynamical behaviour that governs their structural, mechanical, and functional properties. These dynamics arise from the interplay of thermal fluctuations, hydrodynamic interactions, and intermolecular forces, leading to processes such as diffusion, structural relaxation, and self-assembly. Understanding nanoscale transport in these systems is essential for applications ranging from nanomaterials design and drug delivery to biological function and nanofluidics. However, directly probing dynamics on nanometer length scales and microsecond timescales remains experimentally challenging for microscopy and laser scattering and spectroscopy methods, particularly in optically opaque or highly absorbing systems.

X-ray photon correlation spectroscopy (XPCS) provides a powerful tool to study nanoscale dynamics by exploiting temporal fluctuations of coherent X-ray scattering.[1–5] As the X-ray analogue of dynamic light scattering (DLS),[6] XPCS enables access to dynamical processes in systems that are inaccessible to optical techniques, including concentrated dispersions of metallic nanoparticles, and opaque materials. XPCS probes density fluctuations at well-defined momentum transfer vectors, allowing measurements of dynamics on length scales ranging from micrometers down to nanometres. Over the past decade, XPCS has been successfully applied to investigate a wide range of systems, including colloidal suspensions,[7,8] glass-forming liquids and glasses,[9–11] polymers,[12–14] gels,[15–17] and biological matter,[18–20] providing insight into diffusive transport, structural relaxation, and non-equilibrium dynamics.[5]

[a] *Deutsches Elektronen-Synchrotron DESY, Notkestr. 85, 22607 Hamburg, Germany. E-mail: felix.lehmkuehler@desy.de*
[b] *Center for Hybrid Nanostructures, Universität Hamburg, 22761 Hamburg, Germany*
[c] *Department of Physics and Astronomy "Galileo Galilei", University of Padova, Via Marzolo 8, 35121 Padova, Italy*
[d] *ESRF, The European Synchrotron, 71 Avenue des Martyrs, 38043 Grenoble Cedex 9, CS40220, France*
[e] *Department of Physics, University of Siegen, Walter-Flex-Str. 3, 57072 Siegen, Germany*
[f] *Université Grenoble Alpes, CNRS, LIPhy, 38000 Grenoble, France*
[g] *Institut Lumière Matière, Université Claude Bernard Lyon 1, CNRS, Institut Universitaire de France, 69622 Villeurbanne, France*

For nanoscale objects dispersed in low-viscosity solvents such as water, the characteristic timescale is set by Brownian motion set by the diffusion coefficient D. For example, a particle with a radius R = 10 nm in water at room temperature exhibits a Brownian time

$$\tau_B = \frac{R^2}{D} \approx 5\ \mu s, \quad (1)$$

corresponding to the time required to diffuse a length of its own size. Accessing such intrinsic microsecond timescales is essential for probing fundamental transport processes at nanometer length scales. However, conventional synchrotron-based XPCS experiments have been limited to millisecond timescales due to constraints imposed by coherent flux and detector repetition rates,[3,5,21,22] preventing direct observation of fast nanoscale dynamics in particular relevant for low-viscosity liquids.

Recent advances in synchrotron radiation sources, including diffraction-limited storage rings such as the ESRF Extremely Brilliant Source (EBS),[23] have significantly increased the available coherent X-ray flux.[24–26] Because the signal-to-noise ratio in XPCS scales with the square of the coherent flux,[27] these developments extend the accessible dynamical range towards shorter timescales. In parallel, MHz repetition rates available at X-ray free-electron lasers have enabled XPCS measurements down to microsecond and sub-microsecond timescales in soft and biological matter.[28–33] However, such measurements are experimentally demanding due to high peak intensities, pulse-to-pulse fluctuations, and limited beamtime availability at free-electron laser facilities. In contrast, storage rings provide highly stable and continuous X-ray beams ideally suited for equilibrium measurements, provided sufficiently fast and sensitive detectors are available.

The experimentally accessible timescale in XPCS is ultimately determined by detector performance. Conventional hybrid pixel detectors operate at repetition rates in the kHz range,[34–36] limiting measurements to millisecond dynamics. Recent developments in fast hybrid pixel detectors and event-based detection schemes have opened new opportunities for extending XPCS into the microsecond regime.[22,37] In particular, event-driven detectors capable of recording individual photon arrival times enable correlation analysis with sub-microsecond temporal resolution, providing direct access to diffusion dynamics.[38,39]

Gold nanoparticles (AuNPs) are an ideal model system for studying nanoscale transport due to their well-defined size, chemical stability, and strong X-ray scattering contrast. Poly(ethylene glycol) (PEG) coatings provide steric stabilization, prevent aggregation, and ensure well-controlled interparticle interactions.[40,41] PEGylated nanoparticles are widely used in nanomedicine, sensing, and nanofluidics, and serve as model systems for investigating nanoscale transport and hydrodynamic interactions.[42–47] Moreover, their high electron density makes them particularly well suited for XPCS, enabling measurements even at very low particle concentrations.

In addition to serving as model systems, nanoparticles can act as nanoscopic probes of solvent properties. Under dilute conditions, their diffusion coefficient follows the Stokes–Einstein relation, allowing direct determination of the solvent viscosity.[19,48,49] This approach is particularly valuable under extreme thermodynamic conditions, such as supercooling, where conventional macroscopic viscosity measurements become challenging due to the metastability of the system.[50–54]

In this work, we investigate the nanoscale diffusion of dilute PEG-coated gold nanoparticles dispersed in water using synchrotron-based XPCS over a wide temperature range, including water's supercooled regime. We demonstrate that the nanoparticle dynamics follow the Stokes–Einstein–Sutherland relation and provide quantitative access to solvent viscosity. Furthermore, by employing event-based XPCS with modern detectors, we access microsecond dynamics approaching the intrinsic Brownian timescale of nanometer-sized particles. These results establish PEGylated gold nanoparticles as robust nanoscopic probes and highlight the potential of advanced XPCS techniques for investigating fast nanoscale dynamics in soft matter and nanomaterials.

2 Experimental methods

2.1 Samples

The gold nanoparticles (AuNP) were synthesized using the seeded growth method.[55] In this approach, Au seed particles are grown by repeating a series of steps, resulting in different generations of particles with increasing size. This synthesis yields quasi-spherical particles with a narrow size distribution and precise control of the final particle size. The particles were coated with ligand shells made of α-methoxypoly-(ethylene glycol)-ω-(11-mercaptoundecanoate) (PEGMUA) as described in ref. 40. In the present study, PEGMUA ligands with 2 or 5 kDa were used, resulting in a shell thickness of $s \approx 8$ nm and $s \approx 12$ nm, respectively.[41] Different generations and thus different sizes of the particles were studied, an overview is given in Table 1. Some samples were measured at different concentrations to optimize the scattering signal. Before the X-ray scattering experiments, the samples were characterized by dynamic light scattering (DLS) using a Zetasizer by Malvern Panalytical (details are given in the SI). The measured hydrodynamic radii, ranging from 31 nm to 53 nm, are given in Table 1. Additionally, core radii were measured with transmission electron microscopy (TEM) and are shown in the SI.

For the experiment using the event-based read-out of the TEMPUS detector, smaller particles were used. These were synthesized using a modified Turkevich synthesis as described in ref. 56. The AuNP core radius was found to be 6.1 nm. The particles were coated with 2 kDa PEGMUA ligands, resulting in a particle radius of 14.5 nm. All particles were dispersed in milliQ water ($R > 18.2$ MΩ).

2.2 Coherent X-ray scattering experiments

The XPCS experiments were performed at beamline ID02 of ESRF.[24,25] In addition, event-based XPCS studies using the TEMPUS detector[39] were performed at P10 (PETRA III) as well as ID10 of ESRF.

Table 1 Details of the PEGylated AuNP samples: PEG size in kDa, particle radius R in nm and particle volume fraction ϕ. The number is used in case of more than one concentration has been studied. The radius R refers to the sum of core radius and ligand length

Sample	Number	PEG size (kDa)	R (nm)	$\phi \cdot 10^3$
AuNP1	1	5	31	10
	2	5	31	5.2
	3	5	31	2.6
AuNP2	1	5	40	3.8
	2	5	40	1.9
AuNP3		2	41	0.26
		5	45	0.45
AuNP4		2	49	0.19
		5	53	0.10
AuNP5		2	14.5	15

At ID02, the samples were filled in quartz capillaries that were sealed with epoxy glue afterwards and placed in a temperature-controlled Linkam sample stage. The experiment was performed in ultra-small angle X-ray scattering (USAXS) geometry with a sample-detector distance of about 31 m. The photon energy was set to 12.26 keV, the beam size on the sample was 20 μm × 20 μm. An Eiger500k with a maximum repetition rate of 22 kHz was used as detector. The samples were measured at set temperatures between 295 K and 260 K. At lower temperatures, freezing occurred for some samples and limited the experiment to 260 K. Typically, three XPCS runs – each taken at a fresh sample spot – were performed per temperature. Theses consisted of 10 000 frames with an exposure time of 30 μs each. To avoid radiation damage, the threshold dose was carefully determined before in test measurements using different attenuator settings and exposure times. We followed the procedure discussed in ref. 19. XPCS runs were taken using different attenuators and the highest possible intensity showing stationary dynamics has been used. For the ID02 experiment, most samples could be measured without attenuators.

The XPCS experiment using the TEMPUS detector at ID10 (ESRF) has been performed in small-angle scattering geometry using a sample-detector distance of 6.85 m and a beam size of 20 μm × 15 μm. The X-ray energy was set to 8.25 keV. The quartz capillaries filled with the sample were placed in a temperature controllable sample chamber that has been evacuated to reduce the scattering background. XPCS runs consisted of 40 exposures, each 5 s long, per temperature. Each run was taken at a fresh sample spot. Similar to the ID02 experiment, the radiation damage threshold has been checked before and attenuators have been used to limit the exposure to the tolerable minimum. This resulted in an attenuator transmission of 0.02 in this case. Higher intensities would have reached as well the limit of the TEMPUS data transfer.

The approach at P10 was similar to ID10. Here, a sample-detector distance of 5 m and a beam energy of 11.3 keV was used. The beam size was 6.6 μm × 19 μm.

2.3 XPCS method

In XPCS experiments, sample dynamics are probed *via* the intensity autocorrelation functions g_2 that correlates the scattered intensity $I(q, t)$ at a time t with that at time $t + \Delta t$.[5] The g_2 function is related to the correlation function of the field, known as intermediate scattering function $f(q, \Delta t)$, *via* the Siegert relation $g_2(q, \Delta t) = 1 + \beta|f(q, \Delta t)|^2$. Here, q denotes the modulus of the wave vector transfer given by $q = |q| = 4\pi/\lambda \sin(\theta/2)$, with wave length λ and scattering angle θ, and β is the speckle contrast that contains information of the coherence of the X-rays. Thus, g_2 is obtained by[5]

$$g_2(q, \Delta t) = \frac{\langle I(q, t) I(q, t + \Delta t)\rangle}{\langle I(q, t)\rangle^2}, \quad (2)$$

where the averaging is performed over time t and detector pixel belonging to the same q-bin. In case of diffusive dynamics, g_2 can be described by

$$g_2(q, \Delta t) = 1 + \beta \exp(-2\Gamma \Delta t). \quad (3)$$

Here, $\Gamma \equiv 1/\tau$ is the relaxation rate, τ the relaxation time and it is given by

$$\Gamma = Dq^2 = \frac{k_B T}{C\pi\eta R} q^2, \quad (4)$$

with the Stokes–Einstein diffusion coefficient D, depending on temperature T, Boltzmann's constant k_B, viscosity η and particle radius R. The factor C depends on the hydrodynamic boundary conditions; it varies from 4 (full slip) to 6 (no slip).[57,58] Consequently, if temperature, radius and boundary conditions are known and the particle concentration is low, this allows probing the solvent's viscosity. Alternatively, if temperature, radius, and the solvent's viscosity are known, this allows deducing the coefficient C.

While in standard XPCS time series of patterns are analysed following eqn (2), a different approach has to be used for event-based XPCS. Details of the analysis of the TEMPUS data can be found in ref. 38. In short, the TEMPUS detector reports the time of arrival (ToA) and time-over-threshold (ToT) of every photon event per pixel. While the resolution of the ToA is in the (sub-)ns regime,[39] we here focused on the microsecond time scale for the XPCS analysis. Therefore, the events were binned to 500 ns time chunks. In this way effects from the pixel dead time of typically few 100 ns[38] could be avoided. The so-obtained event lists have been analyzed using an event correlator[59] similar to eqn (2) for each pixel individually.

3 Results and discussion

The experimental results are discussed in the following. The average structure by SAXS and dynamics by XPCS are exemplarily shown for sample AuNP4 with 2 kDa PEGMUA ligands in Fig. 1 and 2. All other samples showed analogous results. The results for sample AuNP1 with 5 kDa PEGMUA, representing the smallest studied gold particle size, are given in the SI.

3.1 Structural stability

The azimuthally averaged scattered intensity $I(q)$ was determined by averaging over all pixels at the same scattering vector q. Afterwards, the background was corrected by subtraction of

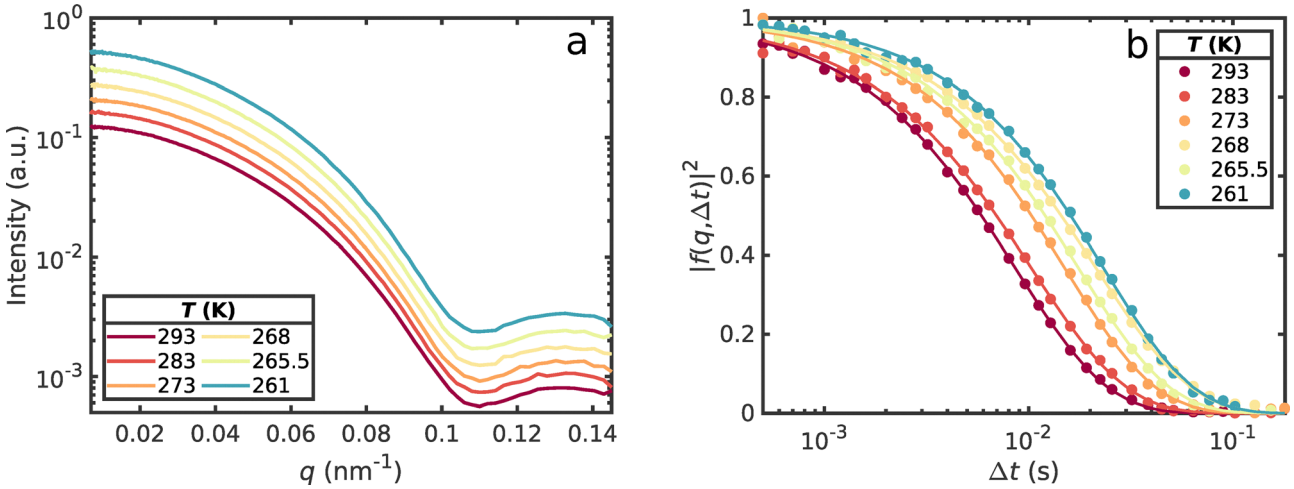

Fig. 1 (a) Azimuthally averaged scattered intensity of AuNP4 with 2 kDa PEGMUA ligands for decreasing temperatures. The intensity profiles have been shifted vertically for clarity. (b) Intermediate scattering functions $|f(q, \Delta t)|^2$ at q = 0.004 nm^{-1} for the same sample and temperatures. The lines are fits to the data with eqn (3).

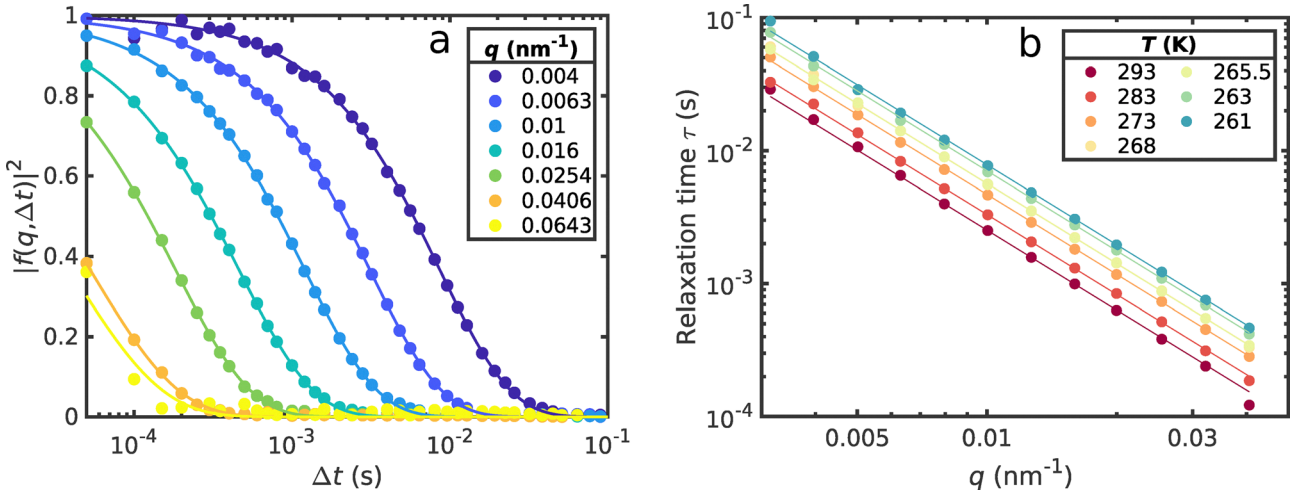

Fig. 2 (a) Intermediate scattering functions $|f(q, \Delta t)|^2$ at T = 293 K for sample AuNP4 with 2 kDa PEGMUA ligands at different values of q. The lines are fits of eqn (3) to the data. (b) Relaxation times τ as a function of q at all measured temperatures T for sample AuNP4 with 2 kDa PEGMUA ligands. The lines correspond to fits of type $\tau = 1/(Dq^2)$.

the intensity obtained from a capillary filled with pure water. The corrected $I(q)$ is shown in Fig. 1(a) at different temperatures T. Since all samples had a volume fraction $\phi \leq 0.015$, the scattered intensity reproduces the particle form factor well. The first minimum of the form factor is visible around $q \approx 0.11$ nm^{-1}. Notably, for all samples, no change in scattered intensity with decreasing temperature is observed. In particular, no indication for a structure factor is visible. At higher concentrations, similar systems exhibit a structure factor peak around $q_{max} \approx 2\pi/R$,[60] *i.e.* $q_{max} \approx 0.064$ nm^{-1} for the particular sample.

3.2 Dynamics

The dynamical properties of the AuNPs were investigated with XPCS. For the ID02 experiment, the speckle contrast was found to be $\beta \approx 0.25$. The intermediate scattering functions were determined from the g_2 functions using eqn (3), and are shown in Fig. 1(b) for different temperatures at q = 0.004 nm^{-1}. With decreasing temperatures, $|f(q, \Delta t)|^2$ shifts to longer times for all samples studied which is connected to the increased viscosity at lower temperatures.

To qualify the type of dynamics further, the intermediate scattering functions are investigated for different q-values. This is exemplarily shown in Fig. 2(a) at T = 293 K. The dynamics become faster with increasing q. Note that, for $q > 0.025$ nm^{-1}, only the long-time tail of the intermediate scattering function could be captured with the time resolution of the experiment. The relaxation times τ are shown in Fig. 2(b) as a function of q for all temperatures studied. It shows a q^{-2} decrease, confirming that the particles undergo Brownian motion. An error-weighted χ^2-fit was used here and throughout the remaining paper. This allows us to extract the diffusion constant D *via* eqn (4).

3.3 Diffusion coefficients and viscosity

The diffusion coefficients D were determined for each individual measurement. Afterwards, an average over all measurements for each temperature and sample was performed. The average was weighted by the errors on D obtained from error propagation, the results are shown in the SI. As expected, the diffusion coefficient is higher for samples with smaller radii. In order to compare diffusion coefficients of all samples, the individual coefficients D have been multiplied by the corresponding particle radius. Thus, $D{\cdot}R$ yields a quantity that depends only on temperature and solvent viscosity. The results are shown in Fig. 3(a). The weighted diffusion coefficients fall together for all samples, independent of the ligand length. An average, weighted by the errors of D, was calculated at each temperature and is shown as black circles and dashed line.

The viscosity was calculated *via* the standard, no-slip boundary Stokes–Einstein equation (eqn (4)) from $D{\cdot}R$ using $C = 6$ and is shown in Fig. 3(b). With decreasing temperature, the viscosity increases exponentially. The viscosity of liquid water in the supercooled regime has been extensively characterized.[50,61,62] Our results reproduce the data from these studies well. The temperature dependence can be described by a power-law model of the form

$$\eta(T) = \eta_0 \left(\frac{T}{T_S} - 1 \right)^{-\varepsilon}. \quad (5)$$

Such power laws have been found to describe viscosity and derived properties very well[50,51] and are connected to mode-coupling theory.[63] Here, η_0 is a scaling amplitude, and T_S denotes the mode-coupling temperature at which the viscosity formally diverges and the liquid becomes non-ergodic. The values reported by Dehaoui *et al.*[50] (T_S = 225.66 K, ε = 1.6438, η_0 = 137.88 μPa s) are shown as red line, providing a good match to the data. This confirms that the Stokes–Einstein relation remains valid for PEGylated Au nanoparticles, also below 273 K. It has to be noted that fitting eqn (5) to a limited amount of data points as in our present study allows a broad range of values especially for the exponent ε. Therefore, the exponent is fixed in some works[51] in order to minimize the fit parameters. Setting the exponent to the value obtained by Dehaoui *et al.*[50] we obtain $\eta_0 = (121 \pm 14)$ μPa s and $T_S = (227.9 \pm 2.2)$ K which is very close to the values of Dehaoui *et al.* The deviations at low temperatures may indicate indeed a smaller C in eqn (5). However, the difference from $C = 6$ is in the range of 1 to 2% and thus within the variation margin of D and in particular R for the different samples, see *e.g.* Fig. 3a. Consequently, the product CR is a constant. This means that both the PEG layer does not become more or less slippery and does not swell for the studied particles sizes and compositions at different temperatures.

3.4 Event-based XPCS

In order to measure the faster dynamics of smaller particles we performed an XPCS experiment using the TEMPUS detector.[39] It is based on the TimePix4 chip for X-ray detection.[64] In contrast to conventional 2D hybrid pixel detectors, it allows an event-based readout of single pixels. It has recently been demonstrated that this mode enables XPCS experiments with sub-μs time resolution.[38] Thus, it allows access to timescales corresponding to diffusion on nanometre length scales. For instance, particles with a radius of 15 nm dispersed in water show a Brownian time, *i.e.* the timescale corresponding to the characteristic time to diffuse over a distance comparable to its radius, of $\tau_B = R^2/D \approx 16$ μs. Even probing larger length scales by accessing smaller q-values in conventional XPCS does not allow access to the relevant microsecond timescales.

Here we chose PEGylated gold particles with a core radius of R_{core} = 6.1 nm, coated with 2 kDa PEG ligands, dispersed in water (sample AuNP5 in Table 1). The system was measured at different temperatures between 298 K and 271 K. Correlation

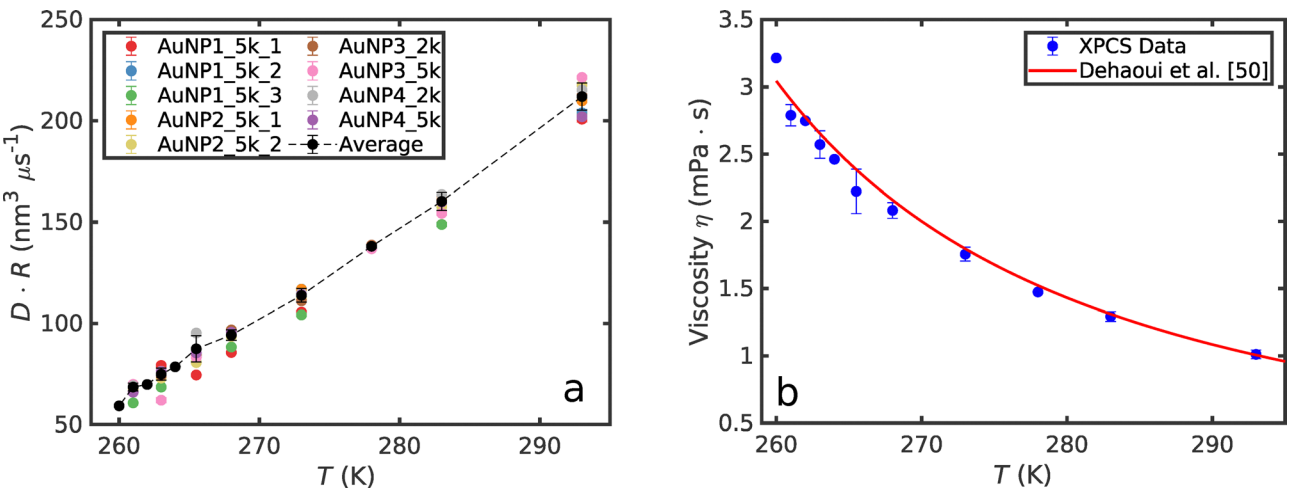

Fig. 3 (a) $D{\cdot}R$ as a function of temperature for all samples. The black dots are the weighted average over all samples. The dashed line connects the black dots linearly as a guide to the eye. (b) Corresponding viscosity η as a function of temperature assuming no slip boundary. The red line shows the power law using the parameters introduced by Dehaoui *et al.*[50] The errorbars are obtained from the error-weighted standard deviation of the measurements of the different samples. Data without error bars (*e.g.* at 260 K) are only measured for a single sample.

functions g_2 from the measurement at 298 K are shown in Fig. 4(a) for different q-values between 0.014 nm^{-1} and 0.08 nm^{-1}. A comparison between the different temperatures is given in Fig. 4(b) for a fixed $q = 0.021\ nm^{-1}$. At short times the TEMPUS data exhibit higher statistical noise. This originates from the microsecond time resolution as well as the significant smaller particles studied here. Nevertheless, the extracted dynamics remain robust. Note that restricting the data to the 10 kHz regime of conventional detectors, the data points are very smooth. All data in both figures could be well described by a single exponential as expected for diffusive particles. The speckle contrast was found to vary between 0.16 to 0.17 in the covered q-range, matching the expectation from beam size, detector pixel size and scattering geometry. Additional TEMPUS data taken from sample AuNP4 are shown in the SI.

The relaxation times obtained from the fits of g_2 are shown in Fig. 4(c) for all temperatures. The data follow the typical q^{-2} behaviour, thus allowing to extract the diffusion coefficient following eqn (4). The results are shown in Fig. 4(d). The data are well described by the Stokes–Einstein model using eqn (5) with $C = 6$ and the values reported by Dehaoui *et al.*[50] for the viscosity. The model reproduces the experimental data very well. The radius of 14.5 nm, corresponding to PEG ligand length of 8.4 nm, matches previous XPCS results on similar sized systems.[65] However, at the lowest temperature we found a deviation from the literature model by approximately 9%. Note that we also observed a deviation for the larger particles discussed above, however, it was in the range of 1 to 2% from the model (differences between experiment and model are highlighted in Fig. S6 and S7). This may suggest that for the small particles where the PEG ligand length is larger than the Au core radius, CR varies as a result of either a changed slip boundary condition or swelling of the PEG shell. For the smallest particles at 272 K, a decrease in hydrodynamic layer thickness of approximately 1 nm would result in the observed 9% deviation. This may arise from temperature-induced deswelling or conformation change of the PEG shell that has been reported for PEG in aqueous solutions.[66] Alternatively, slip

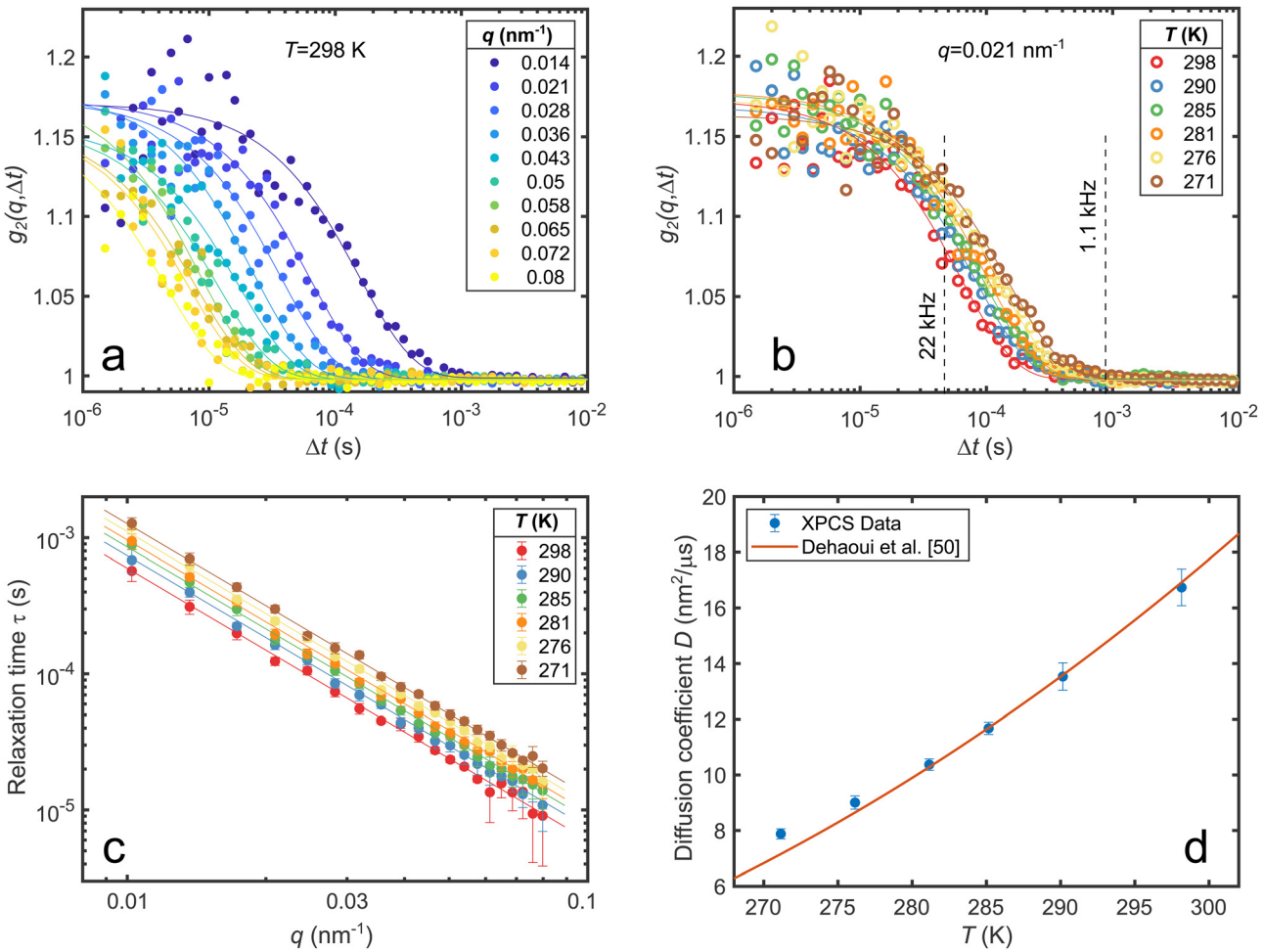

Fig. 4 XPCS results of sample AuNP5 using the TEMPUS detector. (a) g_2 functions at different q probed at $T = 298$ K. The lines represent fits of eqn (3) to the data. (b) g_2 functions at different T probed at $q = 0.021\ nm^{-1}$. The lines represent fits of eqn (3) to the data. The two vertical dashed lines mark the fastest accessible times using the commercial Eiger detectors available at ID10. (c) Relaxation times τ shown as function of q for all temperature studies. The lines represent fits of eqn (4) to the data with D as the only free parameter. (d) Diffusion coefficient D extracted from the fits shown in panel c as a function of T. The line represents the expectation using literature values of η with a particle radius of $R = 14.5$ nm.

effects at the PEG–solvent interface could contribute to the discrepancy, particularly for smaller particles at low temperatures.[45] Independent measures of particles sizes, especially the shell thickness, and more data points at various temperatures and particle sizes are needed to draw a final conclusion.

In a recent DLS study,[51] silica nanoparticles dispersed in water have been used, which represent a charge-stabilized system. In the present work, the concept of such a study is expanded to a soft particle systems with different interparticle interactions, consisting of PEG-coated AuNPs in water. Notably, DLS studies of AuNP dispersion at medium and high concentrations are challenging due to the opacity of the dispersion. The XPCS data here shows that the Stokes–Einstein relation is valid for the diffusion of AuNPs in water down to the supercooled regime with $T \geq 260$ K and sizes of $R \geq 31$ nm.

4 Conclusions

We have demonstrated that XPCS enables quantitative access to nanoscale diffusion of PEGylated gold nanoparticles in water across a wide range of thermodynamic conditions, including water's supercooled regime. The observed Brownian dynamics follow the Stokes–Einstein relation with no slip boundary, and the viscosity extracted from nanoparticle motion agrees quantitatively with established literature values. These results confirm that PEG–coated gold nanoparticles remain structurally and dynamically stable, with no detectable evidence of ligand shell compression or changes in hydrodynamic size within experimental uncertainty, over a wide temperature range. This establishes PEGylated nanoparticles as robust, non-invasive nanoscopic probes for measuring solvent viscosity and nanoscale transport properties.

Critically, by employing event-based XPCS with next-generation detectors, we access microsecond dynamics approaching the intrinsic Brownian timescale of nanometer-sized objects in low-viscosity liquids. This represents a significant advance in experimentally accessible time resolution at storage ring sources and bridges the gap between conventional synchrotron and free-electron laser XPCS capabilities. Importantly, this is achieved under continuous and stable beam conditions ideally suited for equilibrium measurements.

While this study focuses on water properties *via* colloidal tracer particles, extending these methods to more complex soft matter systems such as polymer solutions or biological fluids, will require addressing additional challenges. These include viscoelastic effects, heterogeneous environments, and hydrodynamic interactions,[19,32] which may necessitate adapted correlation analyses or contrast-matching techniques. Nevertheless, the ability to directly probe fast nanoscale dynamics under equilibrium conditions opens new opportunities for studying transport, relaxation, and dynamical heterogeneity in soft matter, nanofluids, and biological systems. These results highlight the strong potential of combining coherent X-ray scattering at modern light sources with event-driven detection to investigate nanoscale dynamics at their fundamental spatiotemporal scales. Furthermore, it demonstrates the impact of XPCS studies at the next-generation light sources[67–70] for soft and hard matter studies and opens the door to studying nanoscale transport in complex fluids, confined geometries, and non-equilibrium systems previously inaccessible at storage ring sources.

Author contributions

Nele N. Striker: conceptualization (supporting), data curation (lead), formal analysis (lead), investigation (equal), methodology (equal), software (equal), validation (equal), visualization (lead), writing – original draft (equal), writing – review & editing (equal). Florian Schulz: conceptualization (supporting), data curation (supporting), investigation (equal), resources (equal), writing – review & editing (equal). Claudia Goy: data curation (supporting), investigation (equal), writing – review & editing (equal). Jonathan Correa: investigation (equal), resources (equal), software (equal), writing – review & editing (equal). Adriana Simancas: investigation (equal), resources (equal), software (equal), writing – review & editing (equal). Francesco Dallari: data curation (supporting), investigation (equal), validation (equal), writing – review & editing (equal). Daniele Marzi: data curation (supporting), investigation (equal), writing – review & editing (equal). Randeer Pratap Gautam: data curation (supporting), investigation (equal), writing – review & editing (equal). Carlos Arauz Moreno: investigation (equal), writing – review & editing (equal). Robert Bauer: investigation (equal), writing – review & editing (equal). William Chevremont: resources (equal), writing – review & editing (equal). Marco Cammarata: investigation (equal), methodology (equal), resources (equal), software (equal), writing – review & editing (equal). Heinz Graafsma: project administration (equal), writing – review & editing (equal). Frédéric Caupin: conceptualization (supporting), data curation (supporting), investigation (equal), writing – review & editing (equal). Felix Lehmkühler: conceptualization (lead), data curation (equal), formal analysis (supporting), funding acquisition (lead), investigation (equal), methodology (equal), project administration (lead), software (equal), supervision (lead), validation (equal), writing – original draft (equal), writing – review & editing (equal).

Conflicts of interest

There are no conflicts to declare.

Data availability

The data that support the findings of this study are available from the corresponding author upon reasonable request. Raw data collected at the ESRF are available at DOI: https://doi.org/10.15151/ESRF-ES-1026511590 and DOI: https://doi.org/10.15151/ESRF-ES-2307850203 and will be made publicly available after the embargo period of three years, in accordance with the ESRF Data Policy.

Supplementary information (SI): details on supporting DLS and TEM measurements, TEM micrographs of the gold particles, data for AuNP1, additional TEMPUS data. See DOI: https://doi.org/10.1039/d6ma00387g.

Acknowledgements

This work is based upon experiments performed at the ID02 and ID10 beamlines at the European Synchrotron Radiation Facility (ESRF), Grenoble, France, under proposals SC-5312 and SC-5741. We acknowledge Deutsches Elektronen-Synchrotron DESY (Hamburg, Germany), a member of the Helmholtz Association HGF, for the provision of experimental facilities. Parts of the measurements of this research were carried out at PETRA III, beamline P10. Beamtime was allocated for proposals under Grant No. I-20250363. We would like to thank Fabian Westermeier for assistance during the experiments. This research was supported in part by the Maxwell computational resources operated at DESY, Hamburg, Germany. N. N. S., R. P. G., and R. P. C. B. acknowledge funding by the Centre for Molecular Water Science (CMWS) within Early Science Projects. F. L., C. G., and R. P. C. B. acknowledge funding by the Helmholtz Association within the framework of the Innovation Pool project "NexUS-AQ" (2025–2027). The research is funded by the Deutsche Forschungsgemeinschaft (DFG, German Research Foundation) as part of the Excellence Strategy of the Federal Government and the federal states – EXC 3120/1 BlueMat: Water-Driven Materials – project number 533771286. C. A.-M. acknowledges the NEutrons and PHotons Elevating Worldwide Science (NEPHEWS) project within Horizon Europe (HORIZON-INFRA-2023-SERV-01) for funding his research stay at PETRA III, DESY (Grant agreement ID: 101131414). F. C. acknowledges funding by Agence Nationale de la Recherche, Grant No. ANR-19-CE30-0035-01. We thank Yuriy Chushkin for input and discussion for the analysis of TEMPUS data and Lars Bocklage for proofreading the manuscript.

Notes and references

1 S. K. Sinha, Z. Jiang and L. B. Lurio, *Adv. Mater.*, 2014, **26**, 7764–7785.
2 A. R. Sandy, Q. Zhang and L. B. Lurio, *Ann. Rev. Mater. Res.*, 2018, **48**, 167–190.
3 A. Madsen, A. Fluerasu and B. Ruta, *Synchrotron Light Sources and Free-Electron Lasers*, Springer International Publishing, 2020, pp. 1989–2018.
4 F. Perakis and C. Gutt, *Phys. Chem. Chem. Phys.*, 2020, **22**, 19443–19453.
5 F. Lehmkühler, W. Roseker and G. Grübel, *Appl. Sci.*, 2021, **11**, 6179.
6 P. Bruce, J. Berne and R. Pecora, *Dynamic Light Scattering: With Applications to Chemistry, Biology, and Physics*, Dover Publications Inc., 2000.
7 A. Fluerasu, P. Kwasniewski, C. Caronna, F. Destremaut, J.-B. Salmon and A. Madsen, *New J. Phys.*, 2010, **12**, 035023.
8 J. Möller and T. Narayanan, *Phys. Rev. Lett.*, 2017, **118**, 198001.
9 B. Ruta, Y. Chushkin, G. Monaco, L. Cipelletti, E. Pineda, P. Bruna, V. M. Giordano and M. Gonzalez-Silveira, *Phys. Rev. Lett.*, 2012, **109**, 165701.
10 J. Li, M. Madhavi, S. Jeppson, L. Zhong, E. M. Dufresne, B. Aitken, S. Sen and R. Kukreja, *J. Phys. Chem. B*, 2022, **126**, 5320–5325.
11 M. Frey, N. Neuber, S. S. Riegler, A. Cornet, Y. Chushkin, F. Zontone, L. M. Ruschel, B. Adam, M. Nabahat, F. Yang, J. Shen, F. Westermeier, M. Sprung, D. Cangialosi, V. Di Lisio, I. Gallino, R. Busch, B. Ruta and E. Pineda, *Nat. Commun.*, 2025, **16**, 4429.
12 A. Papagiannopoulos, T. A. Waigh, A. Fluerasu, C. Fernyhough and A. Madsen, *J. Phys.: Condens. Matter*, 2005, **17**, L279–L285.
13 S. Srivastava, S. Kishore, S. Narayanan, A. R. Sandy and S. R. Bhatia, *J. Polym. Sci., Part B: Polym. Phys.*, 2015, **54**, 752–760.
14 A. Nogales and A. Fluerasu, *Eur. Polym. J.*, 2016, **81**, 494–504.
15 V. Trappe, E. Pitard, L. Ramos, A. Robert, H. Bissig and L. Cipelletti, *Phys. Rev. E: Stat., Nonlinear, Soft Matter Phys.*, 2007, **76**, 051404.
16 Q. Zhang, D. Bahadur, E. M. Dufresne, P. Grybos, P. Kmon, R. L. Leheny, P. Maj, S. Narayanan, R. Szczygiel, S. Ramakrishnan and A. Sandy, *Phys. Rev. Lett.*, 2017, **119**, 178006.
17 A. Jain, F. Schulz, I. Lokteva, L. Frenzel, G. Grübel and F. Lehmkühler, *Soft Matter*, 2020, **16**, 2864–2872.
18 Y. Chushkin, A. Gulotta, F. Roosen-Runge, A. Pal, A. Stradner and P. Schurtenberger, *Phys. Rev. Lett.*, 2022, **129**, 238001.
19 F. Otto, F. Dallari, F. Westermeier, D. C. F. Wieland, W. J. Parak, F. Lehmkühler and F. Schulz, *Aggregate*, 2024, **5**, e483.
20 C. E. P. Silva, A. S. Picco, F. E. Galdino, M. de Burgos Martins de Azevedo, M. Cathcarth, A. R. Passos and M. B. Cardoso, *Nano Lett.*, 2024, **24**, 13293–13299.
21 W. Jo, F. Westermeier, R. Rysov, O. Leupold, F. Schulz, S. Tober, V. Markmann, M. Sprung, A. Ricci, T. Laurus, A. Aschkan, A. Klyuev, U. Trunk, H. Graafsma, G. Grübel and W. Roseker, *IUCrJ*, 2021, **8**, 124–130.
22 W. Jo, S. Stern, F. Westermeier, R. Rysov, M. Riepp, J. Schmehr, J. Lange, J. Becker, M. Sprung, T. Laurus, H. Graafsma, I. Lokteva, G. Grübel and W. Roseker, *Opt. Express*, 2023, **31**, 3315.
23 P. Raimondi, C. Benabderrahmane, P. Berkvens, J. C. Biasci, P. Borowiec, J.-F. Bouteille, T. Brochard, N. B. Brookes, N. Carmignani, L. R. Carver, J.-M. Chaize, J. Chavanne, S. Checchia, Y. Chushkin, F. Cianciosi, M. Di Michiel, R. Dimper, A. D'Elia, D. Einfeld, F. Ewald, L. Farvacque, L. Goirand, L. Hardy, J. Jacob, L. Jolly, M. Krisch, G. Le Bec, I. Leconte, S. M. Liuzzo, C. Maccarrone, T. Marchial, D. Martin, M. Mezouar, C. Nevo, T. Perron, E. Plouviez, H. Reichert, P. Renaud, J.-L. Revol, B. Roche, K.-B. Scheidt, V. Serriere, F. Sette, J. Susini, L. Torino, R. Versteegen, S. White and F. Zontone, *Commun. Phys.*, 2023, **6**, 82.

24 T. Narayanan, M. Sztucki, T. Zinn, J. Kieffer, A. Homs-Puron, J. Gorini, P. Van Vaerenbergh and P. Boesecke, *J. Appl. Crystallogr.*, 2022, **55**, 98–111.
25 W. Chèvremont, T. Zinn and T. Narayanan, *J. Synchrotron Radiat.*, 2024, **31**, 65–76.
26 A. Cornet, A. Ronca, J. Shen, F. Zontone, Y. Chushkin, M. Cammarata, G. Garbarino, M. Sprung, F. Westermeier, T. Deschamps and B. Ruta, *J. Synchrotron Radiat.*, 2024, **31**, 527–539.
27 P. Falus, L. B. Lurio and S. G. J. Mochrie, *J. Synchrotron Radiat.*, 2006, **13**, 253–259.
28 F. Lehmkühler, F. Dallari, A. Jain, M. Sikorski, J. Möller, L. Frenzel, I. Lokteva, G. Mills, M. Walther, H. Sinn, F. Schulz, M. Dartsch, V. Markmann, R. Bean, Y. Kim, P. Vagovic, A. Madsen, A. P. Mancuso and G. Grübel, *Proc. Natl. Acad. Sci. U. S. A.*, 2020, **117**, 24110–24116.
29 F. Dallari, A. Jain, M. Sikorski, J. Möller, R. Bean, U. Boesenberg, L. Frenzel, C. Goy, J. Hallmann, Y. Kim, I. Lokteva, V. Markmann, G. Mills, A. Rodriguez-Fernandez, W. Roseker, M. Scholz, R. Shayduk, P. Vagovic, M. Walther, F. Westermeier, A. Madsen, A. P. Mancuso, G. Grübel and F. Lehmkühler, *IUCrJ*, 2021, **8**, 775–783.
30 F. Dallari, I. Lokteva, J. Möller, W. Roseker, C. Goy, F. Westermeier, U. Boesenberg, J. Hallmann, A. Rodriguez-Fernandez, M. Scholz, R. Shayduk, A. Madsen, G. Grübel and F. Lehmkühler, *Sci. Adv.*, 2024, **10**, eadm7876.
31 M. Reiser, A. Girelli, A. Ragulskaya, S. Das, S. Berkowicz, M. Bin, M. Ladd-Parada, M. Filianina, H.-F. Poggemann, N. Begam, M. S. Akhundzadeh, S. Timmermann, L. Randolph, Y. Chushkin, T. Seydel, U. Boesenberg, J. Hallmann, J. Möller, A. Rodriguez-Fernandez, R. Rosca, R. Schaffer, M. Scholz, R. Shayduk, A. Zozulya, A. Madsen, F. Schreiber, F. Zhang, F. Perakis and C. Gutt, *Nat. Commun.*, 2022, **13**, 5528.
32 A. Girelli, M. Bin, M. Filianina, M. Dargasz, N. D. Anthuparambil, J. Möller, A. Zozulya, I. Andronis, S. Timmermann, S. Berkowicz, S. Retzbach, M. Reiser, A. M. Raza, M. Kowalski, M. Sayed Akhundzadeh, J. Schrage, C. H. Woo, M. D. Senft, L. F. Reichart, A. Leonau, P. R. Prince, W. Chèvremont, T. Seydel, J. Hallmann, A. Rodriguez-Fernandez, J.-E. Pudell, F. Brausse, U. Boesenberg, J. Wrigley, M. Youssef, W. Lu, W. Jo, R. Shayduk, T. Guest, A. Madsen, F. Lehmkühler, M. Paulus, F. Zhang, F. Schreiber, C. Gutt and F. Perakis, *Nat. Commun.*, 2025, **16**, 10814.
33 N. D. Anthuparambil, M. Dargasz, S. Timmermann, A. Girelli, S. Retzbach, J. Möller, W. Jo, A. M. Raza, A. Leonau, J. Wrigley, F. Unger, M. Bin, P. P. Rajaiah, I. Andronis, W. Chèvremont, J. Hallmann, A. Rodriguez-Fernandez, J.-E. Pudell, F. Brausse, U. Boesenberg, M. Youssef, R. Shayduk, R. Rysov, A. Madsen, F. Lehmkühler, M. Paulus, F. Zhang, F. Perakis, F. Schreiber and C. Gutt, *Proc. Natl. Acad. Sci. U. S. A.*, 2026, **123**, e2519681123.
34 D. Pennicard, S. Lange, S. Smoljanin, J. Becker, H. Hirsemann, M. Epple and H. Graafsma, *J. Instrum.*, 2011, **6**, C11009–C11009.
35 V. Radicci, A. Bergamaschi, R. Dinapoli, D. Greiffenberg, B. Henrich, I. Johnson, A. Mozzanica, B. Schmitt and X. Shi, *J. Instrum.*, 2012, **7**, C02019–C02019.
36 T. Donath, D. Šišak Jung, M. Burian, V. Radicci, P. Zambon, A. N. Fitch, C. Dejoie, B. Zhang, M. Ruat, M. Hanfland, C. M. Kewish, G. A. van Riessen, D. Naumenko, H. Amenitsch, G. Bourenkov, G. Bricogne, A. Chari and C. Schulze-Briese, *J. Synchrotron Radiat.*, 2023, **30**, 723–738.
37 Q. Zhang, E. M. Dufresne, S. Narayanan, P. Maj, A. Koziol, R. Szczygiel, P. Grybos, M. Sutton and A. R. Sandy, *J. Synchrotron Radiat.*, 2018, **25**, 1408–1416.
38 Y. Chushkin, J. Correa, A. Ignatenko, D. Pennicard, S. Lange, S. Fridman, S. Karl, B. Senfftleben, F. Lehmkühler, F. Westermeier, H. Graafsma and M. Cammarata, *J. Synchrotron Radiat.*, 2025, **32**, 1220–1227.
39 J. Correa, A. Ignatenko, D. Pennicard, S. Lange, S. Fridman, S. Karl, L. Lohse, B. Senfftleben, I. Sergeev, S. Velten, D. Prajapat, L. Bocklage, H. Bromberger, A. Samartsev, A. Chumakov, R. Rüffer, J. von Zanthier, R. Röhlsberger and H. Graafsma, *J. Synchrotron Radiat.*, 2024, **31**, 1209–1216.
40 F. Schulz, T. Vossmeyer, N. G. Bastús and H. Weller, *Langmuir*, 2013, **29**, 9897–9908.
41 F. Schulz, J. Möller, F. Lehmkühler, A. J. Smith, T. Vossmeyer, H. Lange, G. Grübel and M. A. Schroer, *Part. Part. Syst. Char.*, 2018, **35**, 1700319.
42 G. Kaul and M. Amiji, *J. Pharm. Sci.*, 2005, **94**, 184–198.
43 J. Suh, K.-L. Choy, S. K. Lai, J. S. Suk, B. C. Tang, S. Prabhu and J. Hanes, *Int. J. Nanomed.*, 2007, **2**, 735–741.
44 J. L. Perry, K. G. Reuter, M. P. Kai, K. P. Herlihy, S. W. Jones, J. C. Luft, M. Napier, J. E. Bear and J. M. DeSimone, *Nano Lett.*, 2012, **12**, 5304–5310.
45 E. A. Mun, C. Hannell, S. E. Rogers, P. Hole, A. C. Williams and V. V. Khutoryanskiy, *Langmuir*, 2013, **30**, 308–317.
46 N. Li, H. Cai, L. Jiang, J. Hu, A. Bains, J. Hu, Q. Gong, K. Luo and Z. Gu, *ACS Appl. Mater. Interfaces*, 2017, **9**, 6865–6877.
47 J. McCright, C. Skeen, J. Yarmovsky and K. Maisel, *Acta Biomater.*, 2022, **145**, 146–158.
48 H. Conrad, F. Lehmkühler, B. Fischer, F. Westermeier, M. A. Schroer, Y. Chushkin, C. Gutt, M. Sprung and G. Grübel, *Phys. Rev. E: Stat., Nonlinear, Soft Matter Phys.*, 2015, **91**, 042309.
49 W. Liu, B. Zheng, X. Yin, X. Yu, Y. Zhang, L. Wiegart, A. Fluerasu, B. L. Armstrong, G. M. Veith and S. R. Bhatia, *ACS Appl. Mater. Interfaces*, 2021, **13**, 14267–14274.
50 A. Dehaoui, B. Issenmann and F. Caupin, *Proc. Natl. Acad. Sci. U. S. A.*, 2015, **112**, 12020–12025.
51 S. Berkowicz and F. Perakis, *Phys. Chem. Chem. Phys.*, 2021, **23**, 25490–25499.
52 P. Ragueneau, F. Caupin and B. Issenmann, *Phys. Rev. E*, 2022, **106**, 014616.
53 A. Mussa, R. Berthelard, F. Caupin and B. Issenmann, *J. Chem. Phys.*, 2023, **159**, 151103.
54 J. Eichler, J. Stefanski, J. M. Roca, I. Daniel, B. Issenmann, C. Valeriani and F. Caupin, *Phys. Rev. Lett.*, 2025, **134**, 134101.
55 N. G. Bastús, J. Comenge and V. Puntes, *Langmuir*, 2011, **27**, 11098–11105.

56 F. Schulz, T. Homolka, N. G. Bastús, V. Puntes, H. Weller and T. Vossmeyer, *Langmuir*, 2014, **30**, 10779–10784.
57 J. A. Hodgdon and F. H. Stillinger, *Phys. Rev. E: Stat. Phys., Plasmas, Fluids, Relat. Interdiscip. Top.*, 1993, **48**, 207–213.
58 J. R. Schmidt and J. L. Skinner, *J. Chem. Phys.*, 2003, **119**, 8062–8068.
59 Y. Chushkin, C. Caronna and A. Madsen, *J. Appl. Crystallogr.*, 2012, **45**, 807–813.
60 M. A. Schroer, F. Schulz, F. Lehmkühler, J. Möller, A. J. Smith, H. Lange, T. Vossmeyer and G. Grübel, *J. Phys. Chem. C*, 2016, **120**, 19856–19861.
61 J. Hallett, *Proc. Phys. Soc.*, 1963, **82**, 1046–1050.
62 A. F. Collings and N. Bajenov, *Metrologia*, 1983, **19**, 61–66.
63 W. Gotze and L. Sjogren, *Rep. Prog. Phys.*, 1992, **55**, 241.
64 X. Llopart, J. Alozy, R. Ballabriga, M. Campbell, R. Casanova, V. Gromov, E. Heijne, T. Poikela, E. Santin, V. Sriskaran, L. Tlustos and A. Vitkovskiy, *J. Instrum.*, 2022, **17**, C01044.
65 F. Schulz, A. Jain, F. Dallari, V. Markmann and F. Lehmkühler, *Soft Matter*, 2024, **20**, 3836–3844.
66 M. Wiśniewska, *J. Am. Ceram. Soc.*, 2007, **90**, 3608–3614.
67 C. G. Schroer, I. Agapov, W. Brefeld, R. Brinkmann, Y.-C. Chae, H.-C. Chao, M. Eriksson, J. Keil, X. Nuel Gavaldà, R. Röhlsberger, O. H. Seeck, M. Sprung, M. Tischer, R. Wanzenberg and E. Weckert, *J. Synchrotron Radiat.*, 2018, **25**, 1277–1290.
68 J. Möller, M. Sprung, A. Madsen and C. Gutt, *IUCrJ*, 2019, **6**, 794–803.
69 C. G. Schroer, H.-C. Wille, O. H. Seeck, K. Bagschik, H. Schulte-Schrepping, M. Tischer, H. Graafsma, W. Laasch, K. Baev, S. Klumpp, R. Bartolini, H. Reichert, W. Leemans and E. Weckert, *Eur. Phys. J. Plus*, 2022, **137**, 1312.
70 J. Strzalka, Z. Jiang, J. Wang, Q. Zhang, E. Dufresne and S. Narayanan, *Struct. Dyn.*, 2025, **12**, A302–A302.